NANO LETTERS

pubs.acs.org/NanoLett Letter

Regulating and Directionally Controlling Electron Emission from Gold Nanorods with Silica Coatings

Fabio Medeghini, Jacob Pettine, Sean M. Meyer, Catherine J. Murphy,* and David J. Nesbitt*

Cite This: *Nano Lett.* 2022, 22, 644–651 Read Online

ACCESS | Metrics & More | Article Recommendations | Supporting Information

ABSTRACT: Dielectric coatings offer a versatile means of manipulating hot carrier emission from nanoplasmonic systems for emerging nanocatalysis and photocathode applications, with uniform coatings acting as regulators and nonuniform coatings providing directional photocurrent control. However, the mechanisms for electron emission through dense and mesoporous silica (SiO_2) coatings require further examination. Here, we present a systematic investigation of photoemission from single gold nanorods as a function of dense versus mesoporous silica coating thicknesses. Studies with dense coatings on gold nanostructures clarify the short (~1 nm) attenuation length responsible for severely reduced transmission through the silica conduction band. By contrast, mesoporous silica is much more transmissive, and a simple geometric model quantitatively recapitulates the electron escape probability through nanoscopic porous channels. Finally, photoelectron velocity map imaging (VMI) studies of nanorods with coating defects verify that photoemission occurs preferentially through the thinner regions, illustrating new opportunities for designing photocurrent distributions on the nanoscale.

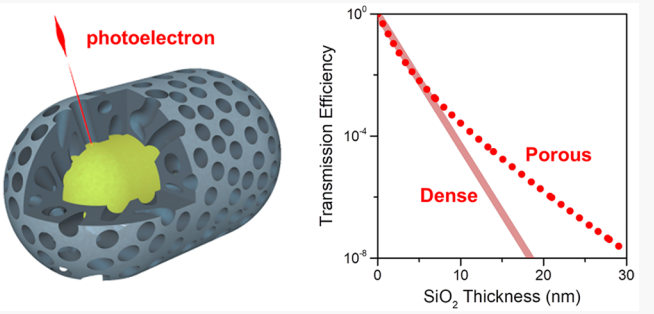

KEYWORDS: *photoemission spectroscopy, hot electrons, mesoporous silica, gold nanorods, single particle*

In recent years, plasmon-induced hot carriers have been widely investigated for applications such as broadband and ultrafast photodetection,[1−4] efficient photovoltaics,[5] product-selective photocatalysis,[6−8] and ultrafast photocathodes.[9−15] Progress in these areas has been made possible by advances in the synthetic[16] and lithographic[17−19] engineering of nanoparticles and structures with surface plasmon resonances (SPRs) that are tuned to desired excitation photon energies,[20] which is accompanied by high charge carrier (electron and hole) densities excited in "hot spot" regions of strong electric field enhancement.[21,22] Plasmonic nanoparticles embedded within semiconductors, for instance, can provide an efficient broadband photovoltaic response, as the excitation photon energy needs only exceed the Schottky barrier at the metal−semiconductor interface rather than the full semiconductor bandgap.[2,23] In gaseous or liquid environments, hot carriers may be transferred to nearby reactant molecules and thereby stimulate efficient product-selective photocatalysis, such as water splitting[6,7] and CO_2 reduction.[8] Additionally, nanoplasmonic systems have demonstrated great promise as fast photodiodes in terahertz nanoelectronics[3,24] and as bright electron beam sources with high spatiotemporal coherence[11,25] for ultrafast electron imaging and X-ray free electron lasers.

Hot electron emission from nanoplasmonic systems is influenced by several factors that affect both the SPR frequency and electric field distributions, including the nanoparticle's size, material, geometry, and surrounding medium. We have shown previously that a high degree of optical control can be achieved via frequency- or polarization-selective excitation of specific plasmonic hot spots[11,16] or by promoting surface versus volume photoexcitation pathways.[26,27] In the present work, dielectric coatings are introduced as a simple yet promising strategy for regulating photocurrent brightness[28,29] as well as spatial and angular distributions. Due to their stability, biocompatibility, and readiness for functionalization with a number of molecules and polymers, SiO_2 coatings have been utilized extensively for biological imaging[30,31] and drug delivery.[32,33] In particular, mesoporous silica has emerged as a particularly suitable coating for applications such as (i) surface-enhanced Raman spectroscopy (SERS),[34,35] where randomly aligned nanoscopic pores can form solvent- or analyte-accessible routes to the plasmonic core,[36,37] and (ii) photocatalysis, where the presence of a mesoporous silica coating increases the thermal stability while allowing facile transient reactant access to the plasmonic surface.[38] Such coatings have also been utilized to measure the distance

Received: September 14, 2021
Revised: December 28, 2021
Published: January 6, 2022

https://doi.org/10.1021/acs.nanolett.1c03569
Nano Lett. 2022, 22, 644−651

dependence of plasmon-enhanced optical processes, such as fluorescence, with nanometer distance precision.[39] Furthermore, these coatings can be grown nonuniformly, for example, encapsulating only the sides or the tips of gold nanorods.[40−45] Plasmon-driven growth of nonuniform coatings has also been demonstrated.[46,47]

In the present work, we explore the regulation of photoemission currents from single gold nanorods with synthetically grown silica coatings. Photoemission from single dense and mesoporous silica coated gold nanorods has been systematically studied as a function of the coating thickness, T, using scanning photoelectron imaging microscopy (SPIM),[48] as described in further detail in SI Section 1. Nanorods were synthesized with a broad range of coating thicknesses (7−21 nm; SI Sections 2 and 3), with the zero-thickness limit evaluated for nanorods coated only with cetyltrimethylammonium bromide (CTAB) ligands (SI Section 1). Representative transmission electron microscopy (TEM) images of mesoporous silica nanorods are presented in Figure 1a and b, and a schematic illustration of the experimental SPIM configuration is presented in Figure 1c. Glass substrates coated in 10 nm indium tin oxide (ITO) ensure high optical transparency for through-sample visible excitation, as well as conductive contact for nanorod reneutralization following a photoemission event. The nanorods were individually addressed by a Ti:sapphire laser (75 MHz, ∼150 fs pulses, 675−1000 nm tuning range) focused to a diffraction-limited (∼500 nm) spot on the sample with a reflective inverse Cassegrain microscope objective (NA = 0.65). Photoelectrons generated within the nanorods travel through the dense or mesoporous silica layer before escaping into free space and are then collected by a velocity map imaging (VMI) electrostatic lens system onto a spatially resolved phosphor-microchannel plate detector.[48]

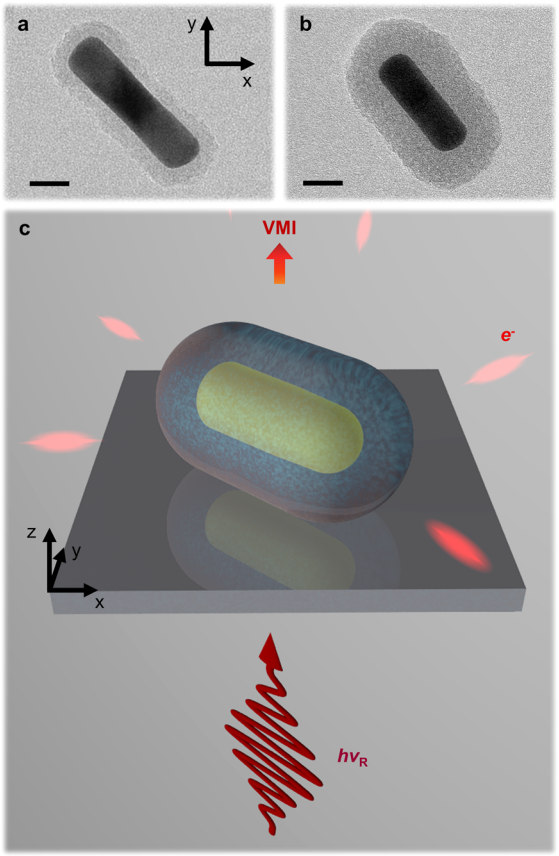

Figure 1. TEM micrographs of gold nanorods embedded in (a) 8 and (b) 17 nm of mesoporous silica (scale bars are 20 nm). (c) Schematic of a silica-coated gold nanorod supported on a glass substrate with an ITO coating. Excitation at resonant energy ($h\nu_R$) from below (red arrow) generates photoelectrons (e^-), which are ejected into free space and collected above on a microchannel plate (MCP).

The impact of silica on the photoemission rate was quantified by studying nanorods of various coating thicknesses, as determined via correlated scanning electron microscopy (SEM) (SI Section 5) and VMI methods. A representative gold nanorod is shown in Figure 2a, which can be described by length (L) and diameter (D) while the mesoporous silica shell is defined by the average conformal thickness, T. Typically, the accurate evaluation of T via SEM becomes challenging for coatings thinner than 10 nm. For the very thinnest silica-coated samples ($T \approx 7$ nm), we therefore report the average thickness as characterized by ensemble TEM measurements. Completely bare ($T = 0$ nm) results reflect average values obtained from measurements of 12 different CTAB-coated nanorods.

The experimental four-photon photoemission (4PPE) dependence on wavelength is shown in Figure 2b for light polarized along the nanorod longitudinal axis and at the peak pulse intensity $I = 1.5$ GW/cm^2. The dependence of the SPR energy, $h\nu_R$, on T and the aspect ratio, L/D, has been calculated via a finite element simulation (SI Section 6), as summarized in Figure 2c. Measured versus predicted SPR positions are in excellent agreement, which the simulations reveal to be due to systematic SPR red-shifts arising from increase in average refractive index of the environment[49] with thicker silica coatings. Logarithmic plots of the intensity dependence measurements for mesoporous silica coated nanorods with different values of T are shown in Figure 2d, which reveal a power law dependence[50] nPPE $= \sigma_n(T)I^n$ that demonstrates a purely four-photon behavior ($n \approx 4$) for the present studies, with y-intercept offsets confirming that nanorods with thicker coatings require higher intensities to maintain similar photoemission rates. Notably, input intensities larger than 1.5 GW/cm^2 augmented by >1000-fold plasmonic intensity enhancements (Figure S7) can approach the optical dielectric breakdown threshold for silica, which is around 10^4 GW/cm^2 based on previous work.[51,52] As characterized via MPPE intensity dependence (e.g., Figure 2d) for each nanorod and otherwise stable signals in time, such effects were not observed in the present perturbative studies with $T \leq 20$ nm. For larger coating thicknesses, the high-input intensities required for sufficient photoemission signals (compensating for attenuation in the silica coatings) may, however, lead to additional strong-field effects and dielectric breakdown physics.

Our primary objective is to systematically quantify the decrease in the n-photon photoemissivity, $\sigma_n(T)$, with increasing T and to help elucidate the photoelectron transmission mechanisms. For further insight into these dynamics, the transmission efficiency ($\sigma_n(T)/\sigma_n(0)$, where $n = 4$) obtained from dense and mesoporous silica nanorods with coatings of varying thickness are summarized in Figure 3a. Increasing T has a dramatic impact on the transmission efficiency, "which decreases by at least six orders of magnitude between $T = 0$ and 20 nm. Most importantly, the T-dependent behaviors and overall photoemission efficiencies for dense versus mesoporous silica coatings are notably different (e.g., by two orders of magnitude at $T = 15$ nm), indicating the

https://doi.org/10.1021/acs.nanolett.1c03569
Nano Lett. 2022, 22, 644−651

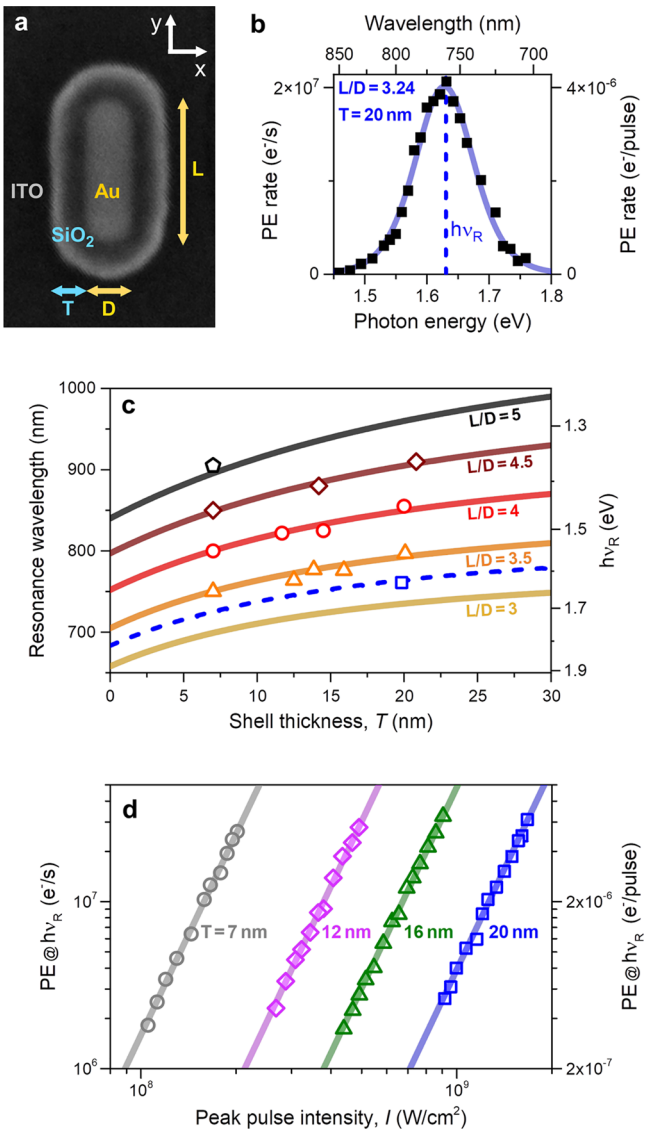

Figure 2. Single nanorod photoemission (PE) characterization. (a) SEM micrograph of a single mesoporous silica coated gold nanorod deposited on ITO. The geometry is described by L, D, and T (81, 25, and 20 nm here, respectively). (b) Corresponding photoemission spectrum (squares, SPIM measurements; solid line, nonlinear Lorentzian fit) of the representative nanorod, which exhibits a resonance at $h\nu_R$ (dashed line). (c) Resonance position as a function of the silica shell thickness T. The value obtained in Figure 2b (see the blue point on the dashed line at T = 20 nm, 1.63 eV) is reported alongside experimental data from representative nanorods with L/D = 3.5, 4, 4.5, and 5 (triangles, circles, diamonds, and pentagons, respectively). Photoemission maxima were predicted by calculating the absorption resonance position for D = 20 nm nanorods of different aspect ratios (solid lines). (d) Photoemission rates of four mesoporous silica coatednanorods with T = 7, 12, 16, and 20 nm (circles, diamonds, triangles, and squares, respectively) optically excited at the SPR with various pulse peak intensities, I, are reproduced well by a simple power law PE = $\sigma_4 I^4$ (solid lines).

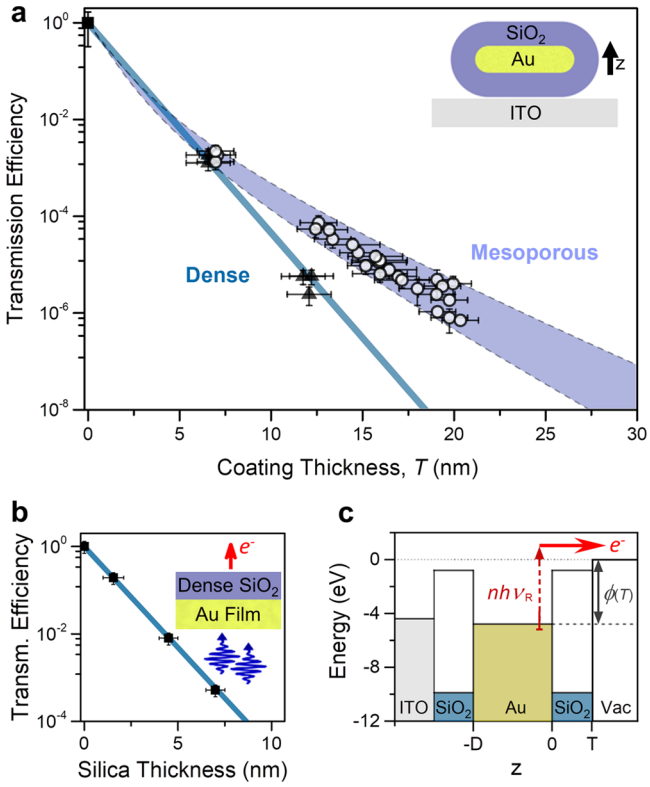

Figure 3. Photoemission dependence on the coating thickness. (a) Transmission efficiency, $\sigma_4(T)/\sigma_4(0)$, of mesoporous silica coated nanorods (open circles) with a range of coating thicknesses. The decreased efficiency with the coating thickness is quantitatively reproduced through a geometric model, with a pore size of L = 3.8 nm and a porosity P = 0.49 ± 0.05 (error bounds are represented by the light blue-shaded area). The value at T = 0 (solid square) is the average of 12 CTAB nanorods and corresponds to a four-photon photoemissivity of $\sigma_4 = 10^{-23}$ $e^-/s/(W/cm^2)$.[4] The transmission efficiency of dense-silica coated nanorods (solid triangles) is fit by an exponential function with an attenuation length of 1.0 ± 0.2 nm (blue line). (b) Transmission efficiency, $\sigma_2(T)/\sigma_2(0)$, of gold films covered with dense silica (squares). The coating effect is fit by an exponential with an attenuation length of 0.94 ± 0.15 nm (line). All vertical error bars represent standard errors of the least-squares intensity-dependence fits. Horizontal error bars represent the uncertainty in the SEM-measured coating thicknesses (nanorods) or the surface roughness (films; SI Section 7). (c) Energy diagram (occupied states are colored) of a silica-coated nanorod on an ITO substrate.

presence of fundamentally different photoelectron transmission mechanisms.

Before proceeding to examine each coating type, we note the influence of the silica coating on the SPR photon energy (Figure 2c), which also indirectly impacts the excess photoelectron kinetic energies (ΔE_n) following nPPE. In general, the photoemission yield is dependent on the square of the excess energy, as described via the Fowler theory[53] nPPE ∝ $\Delta E_n^2 = (nh\nu_R - \phi(T))^2$. This expression also accounts for a thickness-dependent work function, $\phi(T)$ = 4.8−5.7 eV, which is present due to stronger charging effects associated with thicker coatings (see Figure S2). Each of these excess-energy-dependent effects are relatively minor (corrections of order unity) over the energy range studied here but are nevertheless corrected for in the Figure 3a data (see Figure S3). We also note that correlated SEM micrographs unambiguously confirm the avoidance of particle melting in all of these photoemission studies. The deformation threshold for similar mesoporous silica coated nanorods is greater than the maximum fluences utilized in the present studies (3 mJ/cm^2).[54]

We now focus on the transmission dynamics of the dense silica nanorods for which the 4PPE photoemissivity (Figure 3a) can be seen to drop single exponentially with the coating

https://doi.org/10.1021/acs.nanolett.1c03569
Nano Lett. 2022, 22, 644−651

thickness, with an effective attenuation length of λ_{SiO_2} = 1.0 ± 0.2 nm for electrons traveling through the silica conduction band. To preclude any kinetic energy-dependent effects described above, these σ_4 values were measured at a constant excess kinetic energy of $\Delta E_4 \approx 1.2$ eV. Quantitatively identical behavior was found for 2PPE photoemissivity of gold films coated with dense silica of various thicknesses (SI Section 7), which also exhibit pure exponential decay with the same attenuation length λ_{SiO_2} = 0.94 ±0.15 nm (see Figure 3b). To ensure the most accurate comparison with the 4PPE nanorod results, the 2PPE gold film measurements were also performed with an identical two-photon excess energy, $\Delta E_2 \approx 1.2$ eV (i.e., measured coated gold film work functions of 4.8 eV and optical excitation energy of 3 eV). Finally, the $1/e$ attenuation lengths measured for dense-silica-coated gold films and nanorods are also consistent with previous 1PPE studies on gold nanostructures embedded in dense silica, which report λ_{SiO2} = 1.18 ± 0.20 nm for similar excess energies ($\Delta E_1 \approx 1.35$ eV) and attribute this short attenuation length to strong scattering with phonon modes of the SiO_2 bridging oxygen network.[55] Such quantitative agreement indicates that the *n*PPE escape probability is independent of the process order *n*, at least for low-energy electrons, offering more general insight into electron transmission dynamics through nanoscale silica coatings.

The overall impact of dense silica films on photoemission escape is illustrated schematically in the energy diagram of Figure 3c for a silica-coated gold nanorod with a work function of $\phi(T)$ = 4.8 eV (Figure S2). The nanorod is surrounded by a dense silica barrier (9.1 eV bandgap; 0.8 eV electron affinity)[56] and is supported by the ITO substrate (work function ~4.4 eV).[57,58] Optical excitation of the SPR induces a strong electric field enhancement within *the volume* and at the surface of the nanorods,[26] producing high densities of hot electrons that are injected into the empty conduction band of the silica. These hot electrons then travel ballistically through the conduction band with an effective attenuation length,λ_{SiO_2}, losing energy primarily via electron−phonon scattering.[55] The hot electrons that reach the silica−vacuum interface with sufficient surface-normal momentum to escape over the barrier are emitted into free space. Note that the silica does not serve as a tunnel barrier here.

In contrast with dense silica, electron transmission through mesoporous silica can additionally occur via free-space propagation through randomly aligned pores. As a result, the mesoporous silica transmission efficiency is always greater than that of dense silica (seen in Figure 3a). Furthermore, mesoporous silica also exhibits a nonsingle-exponential behavior with the coating thickness and significantly deviates from the dense silica results at large values of T. This indicates that modeling photoelectron transport through mesoporous silica coatings with a single medium-averaged attenuation length would not reliably capture the transmission dynamics, as shown in Figure S10. Instead, and as described in detail below, we find that transmission through mesoporous silica within the volume and at the with a simple geometric model, which indeed can recapitulate the experimental results with quantitative accuracy (reduced χ^2 = 1.1; see residuals in Figure S10). Furthermore, this geometric model is characterized by only two physically motivated or constrained parameters. The first is the average pore size, which is fixed at 3.8 nm based on previous investigations.[36] Direct comparison with this work is possible as our synthesis protocol is based on the same surfactant (CTAB), which defines the pore size. The second is the silica porosity, P, specifically the volumetric pore-to-bulk silica fraction, which serves as the single fit parameter and is 0.49 ± 0.05. It is worth noting that this is consistent within the uncertainty with the porosity value of 0.54 extracted from classic Brunauer−Emmett−Teller methods for surface area measurements of similar mesoporous silica coated nanorods.[36] We also note that residual organics likely remain in the pores[37] despite repeated centrifugation and redispersion of the nanorods in various solvents (SI Section 2). Inelastic scattering and electron trapping by these disordered organic molecules may further reduce the transmission efficiencies through the mesoporous silica coatings, although the significant increase in transmission through the mesoporous versus dense silica and good agreement with the vacuum pore model suggest such scattering effects are weak (i.e., with effective attenuation lengths $\gg \lambda_{SiO_2}$ = 1 nm).

We interpret the thickness-dependent photocurrent attenuation of the mesoporous silica with the help of a disordered pore model, which is illustrated in Figure 4. For simplicity, the pores are treated as randomly distributed cubic elements

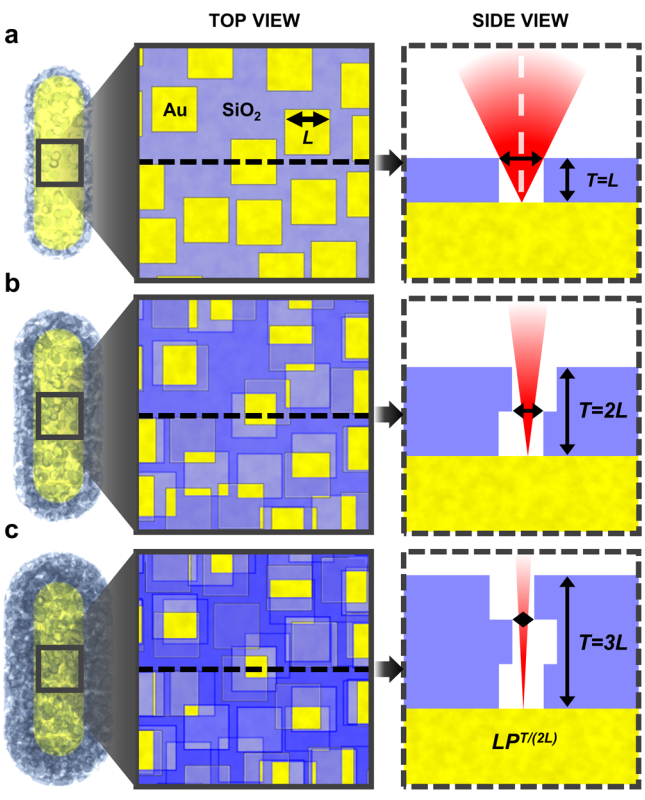

Figure 4. Geometric model of photoelectron transmission through randomly aligned pores. (a) Illustration of a mesoporous silica nanorod with $T = L$. The top view of the 20 × 20 nm^2 gold surface is coated with mesoporous silica, T = 3.8 nm. Cubic pores of edge length L = 3.8 nm cover a portion of Au equal to the porosity P = 0.49. The side view along the dashed line shows photoelectrons (red) constrained by a channel of width L. (b) The introduction of a second layer of mesoporous silica reduces the visible gold area to P^2 = 0.24, narrowing the emission angle. (c) A third layer of mesoporous silica narrows the uncoated gold area to P^3 = 0.12, illustrating how random organization leads to a rapid reduction of the aperture (horizontal arrows) with T.

https://doi.org/10.1021/acs.nanolett.1c03569
Nano Lett. 2022, 22, 644−651

(cylindrical in Figure S4) of dimension L arranged in overlapping sheets, forming $N \approx T/L$ complete layers of mesoporous silica. This is a simplified representation of the interweaving porous structure that nonetheless serves to capture the essential geometric features for the electron transmission dynamics. We initially approximate the silica as nontransmissive, blocking any incident electrons from escaping. The simplest $N = 1$ case ($T = L$) is considered in Figure 4a, where the cubic pores are assumed to take on random coordinates consistent with a bulk porosity P and the absence of long-range order observed in X-ray diffraction experiments on similar mesoporous silica nanorods.[36] The top view of a 20×20 nm^2 flat gold area is covered in mesoporous silica with pores of $L = 3.8$ nm and a porosity of $P = 0.49$. Such a geometry limits the visible gold surface (yellow), corresponding to a decrease in the uncoated gold photoemissivity, $\sigma_4(0)$, by a factor P. A side-view slice of the system is also shown in Figure 4a, where the photoelectrons emitted from the gold surface are constrained by the silica sidewalls. If we approximate the photoemission from the gold surface to be independent of emission angle, the yield may be quantified through the solid angle subtended by the square area of side L as follows:

$$\Omega = 4 \sin^{-1}\left[\frac{L^2}{(L^2 + 4T^2)}\right] \tag{1}$$

It is worth noting that the photoemission rates predicted with eq 1 prove to be quite insensitive to moving the photoemission origin to any other point on the gold surface within the pore, as demonstrated in Figure S4. Furthermore, the approximation of uniform emission (compared, for instance, with a Lambertian-type $\cos(\theta)$ emission distribution with respect to the surface normal[48]) introduces negligible error (Figure S4). The n-photon photoemissivity for thin coatings ($T \lesssim L$) is given by

$$\sigma_n(T, P)\Big|_{T\lesssim L} = \sigma_{n,\mathrm{bare}} P \frac{4}{2\pi} \sin^{-1}\left[\frac{L^2}{(L^2 + 4T^2)}\right] \tag{2}$$

Note that this expression goes to $\sigma_{n,\mathrm{bare}}P$ in the $T \to 0$ limit rather than to $\sigma_{n,\mathrm{bare}}$ due to the approximation of perfectly nontransmissive silica. However, this will be corrected below by accounting for the short but finite effective attenuation length in the silica regions.

The geometric configurations for additional pore layers ($N = 2-3$) are shown in Figure 4b and c. The side views show that some of the pores form vertical channels of width L, but their disorder positioning introduces boundaries limiting the transmission. The effect of multiple disordered pore layers can be accounted for via a reduction in the solid angle accessing the average exposed gold area, as seen from the top view. In the top views, the fraction of area with active gold changes by a factor P per added layer, becoming P^2 and P^3 with the introduction of the second and third layers, respectively. Statistically, the overlap of pores with a square section L^2 yields a visible gold square of area $L^2P^{T/L}$.

Extending this treatment to take the effects of multiple disordered layers into account, we can generalize the photoemissivity of eq 2 to

$$\sigma_n(T, P) = \sigma_{n,\mathrm{bare}} P^{(1+T/L)} \frac{2}{\pi} \sin^{-1}\left[\frac{L^2P^{T/L}}{L^2P^{T/L} + 4T^2}\right] \tag{3}$$

Due to its geometric nature, eq 3 is independent of the multiphoton excitation process and remains valid for all process orders. For $T \gg L$, eq 3 can be approximated as

$$\sigma_n(T, P)\Big|_{T\gg L} \approx \sigma_{n,\mathrm{bare}} \frac{1}{2\pi} \frac{L^2P^{(1+2T/L)}}{T^2} \tag{4}$$

which predicts a rapid decay with T (since $P < 1$). Remarkably, the model predictions are essentially independent of the choice of pore geometry, as explicitly demonstrated in Figure S4. For small thicknesses ($T < 2$ nm), eq 3 does not adequately describe the phenomenon, as transport through the dense silica (with $\lambda_{SiO_2} \approx 1$ nm) becomes appreciable. Therefore, a more complete analytical expression for the photoemissivity of mesoporous-silica nanorods is instead found by summing the two contributions (plotted separately in Figure S5),

$$\sigma_{n,\mathrm{tot}}(T, P) = \sigma_n(T, P) + \sigma_n(T, 1 - P)\mathrm{e}^{-T/\lambda_{SiO_2}} \tag{5}$$

Least-squares fitting yields a porosity of $P = 0.49 \pm 0.05$, which is in excellent agreement with previous estimates.[33] Notably, the two terms of eq 5 describe vacuum-only and silica-only emission channels. Hybrid routes (e.g., alternating vacuum−silica−vacuum) were explored via numerical modeling, as shown in Figure S6, and were found to be negligible due to a combination of the 1 nm effective mean free path in silica and the significant angle-dependent quantum reflectance at each interface including, for instance, escape cone effects.

In addition to uniform silica coatings, we can also monitor the angular distributions of photoelectrons emitted through nonuniform coatings via momentum-resolved 2D VMI.[48] A selection of SEM micrographs are presented in Figure 5 along with their corresponding photoelectron velocity maps. For a uniform mesoporous silica coating (Figure 5a), the corresponding VMI appears nearly isotropic with respect to the azimuthal angle. This is different from recent results with CTAB-coated gold nanorods[26] due to the larger surface/volume field ratio promoted by the silica coating, as discussed in Figure S7.

As a final demonstration to highlight possibilities for nanoscale angular and spatial photocurrent control and design, we investigate several nanorods with random defects (thinner regions) evident in their coatings. Two such nanorods are shown in Figure 5b and c SEMs, with corresponding VMIs demonstrating highly directional emission that is distinctly aligned with physical defects in the silica coatings (see Figure S8). Based on an average shell thickness, their transmission efficiency results are respectively 4.5 and 7.5× larger than our findings for uniformly coated rods (see Figure S9). Thus, while the effect of the silica coatings is quantified statistically in Figure 3 for many different uniformly coated nanorods, it is also directly visualized in Figure 5 for individual nanorods with nonuniform coatings. While random defects in the silica-coated nanorods have been examined herein with correlated SEM and VMI capabilities to demonstrate such effects, the results are in fact relevant to actual device applications, with designer anisotropic nanoparticle coatings already being demonstrated to be a well-developed technology.[41,59] Thus, these results illustrate new and realistic opportunities for directionally tailoring photocurrents in nanocathode, nanoelectronic, photovoltaic, and photocatalytic hot carrier applications.

In conclusion, photoemission from resonantly excited gold nanorods has been characterized for dense and mesoporous

https://doi.org/10.1021/acs.nanolett.1c03569
Nano Lett. 2022, 22, 644−651

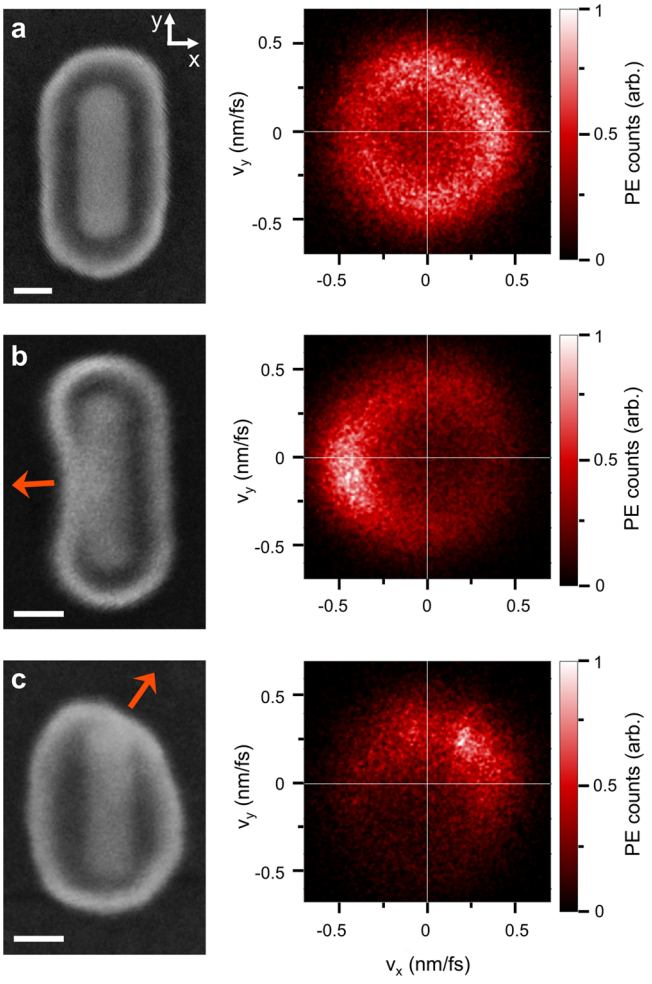

Figure 5. SEM micrographs of single mesoporous silica coated nanorods (scale bars are 20 nm) and associated photoelectron velocity maps. (a) The uniform coating of the nanorod from Figure 2a leads to nearly isotropic photoemission. (b and c) Random defect regions with thinner coatings enhance the photoelectron transmission along the corresponding direction (red arrows).

silica coatings of different thicknesses. Dense silica coatings exhibit an exponential drop in the transmission efficiency with the increasing thickness, with the ∼1 nm attenuation length yielding a dramatic reduction in transmission compared with bare nanorods, even for few-nanometer coatings. A less dramatic (yet still considerable) nonexponential decay with the mesoporous silica thickness is attributed to free-space transmission of the photoelectrons through randomly aligned nanoscopic pores, as elucidated via simple geometric modeling with excellent quantitative agreement. Either mesoporous or dense silica coating strategies may be utilized to regulate or essentially block hot carrier transfer or emission to prevent unwanted chemical transformations in surface- or tip-enhanced Raman spectroscopy studies[29,60] or to distinguish between hot carrier and thermal effects in plasmonic catalysts. Furthermore, preliminary angle-resolved photoemission studies of nanorods with random defects in the mesoporous silica coatings have been used to demonstrate *directional* photocurrent distributions systematically aligned with the thinner coating defect regions. Dielectric coatings may thus be tailored for nanoscale site-selective catalysis or to enhance photoemission directionality in emerging plasmonic nanocathode and nanoelectronics applications.

■ ASSOCIATED CONTENT

Supporting Information

The Supporting Information is available free of charge at https://pubs.acs.org/doi/10.1021/acs.nanolett.1c03569.

Synthesis of cetyltrimethylammonium bromide (CTAB) gold nanorods, coating of dense silica and mesoporous silica on gold nanorods, scanning photoelectron imaging microscopy, scanning electron microscopy, finite element method, electron beam evaporation and film characterization, photoemission polarization dependence of single nanorods, experimental determination of the effective work function, comparison between original and corrected photoemissivity, impact of geometric approximations in the disordered cubic pores model, and bare and coated nanorod field simulations (PDF)

■ AUTHOR INFORMATION

Corresponding Authors

Catherine J. Murphy − *Department of Chemistry, University of Illinois at Urbana−Champaign, Urbana, Illinois 61801, United States; Materials Research Laboratory, University of Illinois at Urbana−Champaign, Urbana, Illinois 61801, United States;* orcid.org/0000-0001-7066-5575; Email: murphycj@illinois.edu

David J. Nesbitt − *JILA, University of Colorado—Boulder and National Institute of Standards and Technology, Boulder, Colorado 80309, United States; Department of Physics and Department of Chemistry, University of Colorado—Boulder, Boulder, Colorado 80309, United States;* orcid.org/0000-0001-5365-1120; Email: djn@jila.colorado.edu

Authors

Fabio Medeghini − *JILA, University of Colorado—Boulder and National Institute of Standards and Technology, Boulder, Colorado 80309, United States*

Jacob Pettine − *JILA, University of Colorado—Boulder and National Institute of Standards and Technology, Boulder, Colorado 80309, United States; Department of Physics, University of Colorado—Boulder, Boulder, Colorado 80309, United States*

Sean M. Meyer − *Department of Chemistry, University of Illinois at Urbana−Champaign, Urbana, Illinois 61801, United States;* orcid.org/0000-0003-0771-5095

Complete contact information is available at: https://pubs.acs.org/10.1021/acs.nanolett.1c03569

Notes

The authors declare no competing financial interest.

■ ACKNOWLEDGMENTS

Photoemission studies in the D.J.N. laboratory have been supported by the Air Force Office of Scientific Research (FA9550-15-1-0090) with additional funds for laser development and apparatus construction provided by the National Science Foundation (PHY-1734006). Nanorod synthesis in the C.J.M. laboratory was supported by the National Science Foundation (CHE-1608743 and CHE-2107793).

REFERENCES

(1) Ghobadi, T. G. U.; Ghobadi, A.; Özbay, E.; Karadas, F. Strategies for Plasmonic Hot-Electron-Driven Photoelectrochemical Water Splitting. *ChemPhotoChem.* **2018**, *2* (3), 161−182.

(2) Knight, M. W.; Sobhani, H.; Nordlander, P.; Halas, N. J. Photodetection with Active Optical Antennas. *Science* **2011**, *332* (6030), 702−704.

(3) Dorodnyy, A.; Salamin, Y.; Ma, P.; Plestina, J. V.; Lassaline, N.; Mikulik, D.; Romero-Gomez, P.; Morral, A. F. I.; Leuthold, J. Plasmonic Photodetectors. *IEEE J. Sel. Top. Quant.* **2018**, *24* (6), 1−13.

(4) Brongersma, M. L.; Halas, N. J.; Nordlander, P. Plasmon-Induced Hot Carrier Science and Technology. *Nat. Nanotechnol.* **2015**, *10* (1), 25−34.

(5) Clavero, C. Plasmon-Induced Hot-Electron Generation at Nanoparticle/Metal-Oxide Interfaces for Photovoltaic and Photocatalytic Devices. *Nat. Photonics* **2014**, *8* (2), 95−103.

(6) Shi, X.; Ueno, K.; Oshikiri, T.; Sun, Q.; Sasaki, K.; Misawa, H. Enhanced Water Splitting under Modal Strong Coupling Conditions. *Nat. Nanotechnol.* **2018**, *13* (10), 953−958.

(7) Maeda, K.; Domen, K. Photocatalytic Water Splitting: Recent Progress and Future Challenges. *J. Phys. Chem. Lett.* **2010**, *1* (18), 2655−2661.

(8) Yu, S.; Wilson, A. J.; Heo, J.; Jain, P. K. Plasmonic Control of Multi-Electron Transfer and C−C Coupling in Visible-Light-Driven CO_2 Reduction on Au Nanoparticles. *Nano Lett.* **2018**, *18* (4), 2189−2194.

(9) Bainbridge, A.; Bryan, W. Velocity Map Imaging of Femtosecond Laser Induced Photoelectron Emission from Metal Nanotips. *New J. Phys.* **2014**, *16* (10), 103031.

(10) Park, D. J.; Piglosiewicz, B.; Schmidt, S.; Kollmann, H.; Mascheck, M.; Lienau, C. Strong Field Acceleration and Steering of Ultrafast Electron Pulses from a Sharp Metallic Nanotip. *Phys. Rev. Lett.* **2012**, *109* (24), 244803.

(11) Pettine, J.; Choo, P.; Medeghini, F.; Odom, T. W.; Nesbitt, D. J. Plasmonic Nanostar Photocathodes for Optically-Controlled Directional Currents. *Nat. Commun.* **2020**, *11* (1), 1367.

(12) Yanagisawa, H.; Hafner, C.; Doná, P.; Klöckner, M.; Leuenberger, D.; Greber, T.; Osterwalder, J.; Hengsberger, M. Laser-Induced Field Emission from a Tungsten Tip: Optical Control of Emission Sites and the Emission Process. *Phys. Rev. B* **2010**, *81* (11), 115429.

(13) Cho, B.; Ichimura, T.; Shimizu, R.; Oshima, C. Quantitative Evaluation of Spatial Coherence of the Electron Beam from Low Temperature Field Emitters. *Phys. Rev. Lett.* **2004**, *92* (24), 246103.

(14) Ehberger, D.; Hammer, J.; Eisele, M.; Krüger, M.; Noe, J.; Högele, A.; Hommelhoff, P. Highly Coherent Electron Beam from a Laser-Triggered Tungsten Needle Tip. *Phys. Rev. Lett.* **2015**, *114* (22), 227601.

(15) Meier, S.; Higuchi, T.; Nutz, M.; Högele, A.; Hommelhoff, P. High Spatial Coherence in Multiphoton-Photoemitted Electron Beams. *Appl. Phys. Lett.* **2018**, *113* (14), 143101.

(16) Hrelescu, C.; Sau, T. K.; Rogach, A. L.; Jäckel, F.; Laurent, G.; Douillard, L.; Charra, F. Selective Excitation of Individual Plasmonic Hotspots at the Tips of Single Gold Nanostars. *Nano Lett.* **2011**, *11* (2), 402−407.

(17) Kasani, S.; Curtin, K.; Wu, N. A Review of 2D and 3D Plasmonic Nanostructure Array Patterns: Fabrication, Light Management and Sensing Applications. *Nanophotonics* **2019**, *8* (12), 2065−2089.

(18) Rybka, T.; Ludwig, M.; Schmalz, M. F.; Knittel, V.; Brida, D.; Leitenstorfer, A. Sub-Cycle Optical Phase Control of Nanotunnelling in the Single-Electron Regime. *Nat. Photonics* **2016**, *10* (10), 667.

(19) Zimmermann, P.; Hötger, A.; Fernandez, N.; Nolinder, A.; Müller, K.; Finley, J. J.; Holleitner, A. W. Toward Plasmonic Tunnel Gaps for Nanoscale Photoemission Currents by On-Chip Laser Ablation. *Nano Lett.* **2019**, *19* (2), 1172−1178.

(20) Schuller, J. A.; Barnard, E. S.; Cai, W.; Jun, Y. C.; White, J. S.; Brongersma, M. L. Plasmonics for Extreme Light Concentration and Manipulation. *Nat. Mater.* **2010**, *9* (3), 193−204.

(21) Awada, C.; Popescu, T.; Douillard, L.; Charra, F.; Perron, A.; Yockell-Lelièvre, H. l. n.; Baudrion, A.-L.; Adam, P.-M.; Bachelot, R. Selective Excitation of Plasmon Resonances of Single Au Triangles by Polarization-Dependent Light Excitation. *J. Phys. Chem. C* **2012**, *116* (27), 14591−14598.

(22) Dombi, P. T.; Hörl, A.; Rácz, P. T.; Márton, I. N.; Trügler, A.; Krenn, J. R.; Hohenester, U. Ultrafast Strong-Field Photoemission from Plasmonic Nanoparticles. *Nano Lett.* **2013**, *13* (2), 674−678.

(23) Nishijima, Y.; Ueno, K.; Yokota, Y.; Murakoshi, K.; Misawa, H. Plasmon-Assisted Photocurrent Generation from Visible to Near-Infrared Wavelength using a Au-Nanorods/TiO_2 Electrode. *J. Phys. Chem. Lett.* **2010**, *1* (13), 2031−2036.

(24) Karnetzky, C.; Zimmermann, P.; Trummer, C.; Duque Sierra, C.; Worle, M.; Kienberger, R.; Holleitner, A. Towards Femtosecond On-Chip Electronics Based On Plasmonic Hot Electron Nano-Emitters. *Nat. Commun.* **2018**, *9* (1), 2471.

(25) Hobbs, R. G.; Yang, Y.; Fallahi, A.; Keathley, P. D.; De Leo, E.; Kärtner, F. X.; Graves, W. S.; Berggren, K. K. High-Yield, Ultrafast, Surface Plasmon-Enhanced, Au Nanorod Optical Field Electron Emitter Arrays. *ACS Nano* **2014**, *8* (11), 11474−11482.

(26) Pettine, J.; Meyer, S. M.; Medeghini, F.; Murphy, C. J.; Nesbitt, D. J. Controlling the Spatial and Momentum Distributions of Plasmonic Carriers: Volume vs Surface Effects. *ACS Nano* **2021**, *15* (1), 1566−1578.

(27) Pettine, J.; Menendez, A. M.; Nesbitt, D. J. Continuous Angular Control Over Anisotropic Photoemission from Isotropic Gold Nanoshells. *J. Chem. Phys.* **2020**, *153* (10), 101101.

(28) Xiong, X.; Zhou, Y.; Luo, Y.; Li, X.; Bosman, M.; Ang, L. K.; Zhang, P.; Wu, L. Plasmon-Enhanced Resonant Photoemission Using Atomically Thick Dielectric Coatings. *ACS Nano* **2020**, *14* (7), 8806−8815.

(29) Takeyasu, N.; Yamaguchi, K.; Kagawa, R.; Kaneta, T.; Benz, F.; Fujii, M.; Baumberg, J. J. Blocking Hot Electron Emission by SiO_2 Coating Plasmonic Nanostructures. *J. Phys. Chem. C* **2017**, *121* (34), 18795−18799.

(30) Chen, Y.-S.; Frey, W.; Kim, S.; Kruizinga, P.; Homan, K.; Emelianov, S. Silica-Coated Gold Nanorods as Photoacoustic Signal Nanoamplifiers. *Nano Lett.* **2011**, *11* (2), 348−354.

(31) Comenge, J.; Fragueiro, O.; Sharkey, J.; Taylor, A.; Held, M.; Burton, N. C.; Park, B. K.; Wilm, B.; Murray, P.; Brust, M.; et al. Preventing Plasmon Coupling Between Gold Nanorods Improves the Sensitivity of Photoacoustic Detection of Labeled Stem Cells in Vivo. *ACS Nano* **2016**, *10* (7), 7106−7116.

(32) An, L.; Wang, Y.; Tian, Q.; Yang, S. Small Gold Nanorods: Recent Advances in Synthesis, Biological Imaging, and Cancer Therapy. *Materials* **2017**, *10* (12), 1372.

(33) Ishtiaq, S.; Shah, K. U.; Ur-Rehman, T.; Ud-Din, F. Gold Nanorods: New Generation Drug Delivery Platform. In *Metal Nanoparticles for Drug Delivery and Diagnostic Applications*; Shah, M. R., Imran, M., Ullah, S., Eds.; Elsevier: Cambridge, MA, 2020; pp 59−84.

(34) Haidar, I.; Lévi, G.; Mouton, L.; Aubard, J.; Grand, J.; Lau-Truong, S.; Neuville, D. R.; Félidj, N.; Boubekeur-Lecaque, L. Highly Stable Silica-Coated Gold Nanorods Dimers for Solution-Based SERS. *Phys. Chem. Chem. Phys.* **2016**, *18* (47), 32272−32280.

(35) Blanco-Formoso, M.; Sousa-Castillo, A.; Xiao, X.; Mariño-Lopez, A.; Turino, M.; Pazos-Perez, N.; Giannini, V.; Correa-Duarte, M. A.; Alvarez-Puebla, R. A. Boosting the Analytical Properties of Gold Nanostars by Single Particle Confinement into Yolk Porous Silica Shells. *Nanoscale* **2019**, *11* (45), 21872−21879.

(36) Gao, Z.; Burrows, N. D.; Valley, N. A.; Schatz, G. C.; Murphy, C. J.; Haynes, C. L. In Solution SERS Sensing Using Mesoporous Silica-Coated Gold Nanorods. *Analyst* **2016**, *141* (17), 5088−5095.

(37) Janicek, B. E.; Hinman, J. G.; Hinman, J. J.; Bae, S. H.; Wu, M.; Turner, J.; Chang, H.-H.; Park, E.; Lawless, R.; Suslick, K. S.; Murphy, C. J.; Huang, P. Y. Quantitative Imaging of Organic Ligand Density

https://doi.org/10.1021/acs.nanolett.1c03569
Nano Lett. 2022, 22, 644−651

on Anisotropic Inorganic Nanocrystals. *Nano Lett.* **2019**, *19* (9), 6308−6314.
(38) Zhang, T.; Zhao, H.; He, S.; Liu, K.; Liu, H.; Yin, Y.; Gao, C. Unconventional Route to Encapsulated Ultrasmall Gold Nanoparticles for High-Temperature Catalysis. *ACS Nano* **2014**, *8* (7), 7297−7304.
(39) Abadeer, N. S.; Brennan, M. R.; Wilson, W. L.; Murphy, C. J. Distance and Plasmon Wavelength Dependent Fluorescence of Molecules Bound to Silica-Coated Gold Nanorods. *ACS Nano* **2014**, *8* (8), 8392−8406.
(40) Anderson, B. D.; Wu, W.-C.; Tracy, J. B. Silica Overcoating of CdSe/CdS Core/Shell Quantum Dot Nanorods with Controlled Morphologies. *Chem. Mater.* **2016**, *28* (14), 4945−4952.
(41) Burrows, N. D.; Vartanian, A. M.; Abadeer, N. S.; Grzincic, E. M.; Jacob, L. M.; Lin, W.; Li, J.; Dennison, J. M.; Hinman, J. G.; Murphy, C. J. Anisotropic Nanoparticles and Anisotropic Surface Chemistry. *J. Phys. Chem. Lett.* **2016**, *7* (4), 632−641.
(42) Huang, C.-M.; Chung, M.-F.; Souris, J. S.; Lo, L.-W. Controlled Epitaxial Growth of Mesoporous Silica/Gold Nanorod Nanolollipops and Nanodumbbells. *APL Mater.* **2014**, *2* (11), 113312.
(43) Rowe, L. R.; Chapman, B. S.; Tracy, J. B. Understanding and Controlling the Morphology of Silica Shells on Gold Nanorods. *Chem. Mater.* **2018**, *30* (18), 6249−6258.
(44) Wang, F.; Cheng, S.; Bao, Z.; Wang, J. Anisotropic Overgrowth of Metal Heterostructures Induced by a Site-Selective Silica Coating. *Angew. Chem., Int. Ed.* **2013**, *52* (39), 10344−10348.
(45) Wu, B.; Liu, D.; Mubeen, S.; Chuong, T. T.; Moskovits, M.; Stucky, G. D. Anisotropic Growth of TiO_2 onto Gold Nanorods for Plasmon-Enhanced Hydrogen Production from Water Reduction. *J. Am. Chem. Soc.* **2016**, *138* (4), 1114−1117.
(46) Hobbs, R. G.; Putnam, W. P.; Fallahi, A.; Yang, Y.; Kärtner, F. X.; Berggren, K. K. Mapping Photoemission and Hot-Electron Emission from Plasmonic Nanoantennas. *Nano Lett.* **2017**, *17* (10), 6069−6076.
(47) Wang, Y.; Wang, S.; Zhang, S.; Scherman, O. A.; Baumberg, J. J.; Ding, T.; Xu, H. Plasmon-Directed Polymerization: Regulating Polymer Growth with Light. *Nano Res.* **2018**, *11* (12), 6384−6390.
(48) Pettine, J.; Grubisic, A.; Nesbitt, D. J. Angle- and Momentum-Resolved Photoelectron Velocity Map Imaging Studies of Thin Au Film and Single Supported Au Nanoshells. *J. Phys. Chem. C* **2018**, *122* (7), 3970−3984.
(49) Link, S.; Mohamed, M.; El-Sayed, M. Simulation of the Optical Absorption Spectra of Gold Nanorods as a Function of Their Aspect Ratio and the Effect of the Medium Dielectric Constant. *J. Phys. Chem. B* **1999**, *103* (16), 3073−3077.
(50) Zhou, S.; Chen, K.; Cole, M. T.; Li, Z.; Chen, J.; Li, C.; Dai, Q. Ultrafast Field-Emission Electron Sources Based on Nanomaterials. *Adv. Mater.* **2019**, *31* (45), 1805845.
(51) Deng, Y.; Xie, X.; Xiong, H.; Leng, Y.; Cheng, C.; Lu, H.; Li, R.; Xu, Z. Optical Breakdown for Silica and Silicon with Double Femtosecond Laser Pulses. *Opt. Express* **2005**, *13* (8), 3096−3103.
(52) Schaffer, C. B.; Brodeur, A.; Mazur, E. Laser-Induced Breakdown and Damage in Bulk Transparent Materials Induced by Tightly Focused Femtosecond Laser Pulses. *Meas. Sci. Technol.* **2001**, *12* (11), 1784.
(53) Fowler, R. H. The Analysis of Photoelectric Sensitivity Curves for Clean Metals at Various Temperatures. *Phys. Rev.* **1931**, *38* (1), 45−56.
(54) Albrecht, W.; Deng, T.-S.; Goris, B.; van Huis, M. A.; Bals, S.; van Blaaderen, A. Single Particle Deformation and Analysis of Silica-Coated Gold Nanorods Before and After Femtosecond Laser Pulse Excitation. *Nano Lett.* **2016**, *16* (3), 1818−1825.
(55) Ballarotto, V.; Breban, M.; Siegrist, K.; Phaneuf, R.; Williams, E. Photoelectron Emission Microscopy of Ultrathin Oxide Covered Devices. *J. Vac. Sci. Technol. B* **2002**, *20* (6), 2514−2518.
(56) Astašauskas, V.; Bellissimo, A.; Kuksa, P.; Tomastik, C.; Kalbe, H.; Werner, W. S. Optical and Electronic Properties of Amorphous Silicon Dioxide by Single and Double Electron Spectroscopy. *J. Electron. Spectrosc.* **2020**, *241*, 146829.
(57) Park, Y.; Choong, V.; Gao, Y.; Hsieh, B. R.; Tang, C. W. Work Function of Indium Tin Oxide Transparent Conductor Measured by Photoelectron Spectroscopy. *Appl. Phys. Lett.* **1996**, *68* (19), 2699−2701.
(58) Sugiyama, K.; Ishii, H.; Ouchi, Y.; Seki, K. Dependence of Indium−Tin−Oxide Work Function on Surface Cleaning Method as Studied by Ultraviolet and X-ray Photoemission Spectroscopies. *J. Appl. Phys.* **2000**, *87* (1), 295−298.
(59) Mubeen, S.; Lee, J.; Singh, N.; Krämer, S.; Stucky, G. D.; Moskovits, M. An Autonomous Photosynthetic Device in which All Charge Carriers Derive from Surface Plasmons. *Nat. Nanotechnol.* **2013**, *8* (4), 247−251.
(60) Szczerbinski, J.; Yin, H.; Zhang, Y.-J.; Zhang, F.-L.; Li, J.-F.; Zenobi, R. Preserving Plasmonic Nanostructures from Laser-Induced Deactivation by a Protective Dielectric Shell. *J. Phys. Chem. C* **2020**, *124* (11), 6385−6394.

https://doi.org/10.1021/acs.nanolett.1c03569
Nano Lett. 2022, 22, 644−651